Bohnhoff, M., Zoback, M. D. (2010): Oscillation of fluid-filled cracks triggered by degassing of CO2 due to leakage along wellbores. - Journal of Geophysical Research, 115, B11305

DOI: 10.1029/2010JB000848

Oscillation of fluid-filled cracks triggered by degassing of CO_2 due to leakage along wellbores

Marco Bohnhoff[1,2] and Mark D. Zoback[1]

Received 7 January 2010; revised 7 June 2010; accepted 14 July 2010; published 6 November 2010.

[1] We present evidence for a seismic source associated with degassing CO_2 during leakage along two wellbores instrumented with arrays of downhole seismometers. More than 200 microseismic events were detected in direct vicinity of the monitoring wells. The observed seismic waves are dominantly P waves and tube waves, with no (or extremely weak S) shear waves. The waveforms of these events indicate extremely rapid amplitude decays with distance across the arrays, consistent with the seismometers being in the near field of the seismic source. The frequency characteristics, first-motion polarities and S to P amplitude ratios suggest a single force source mechanism. Because the seismic arrays were located at the depth where the density of ascending CO_2 changes most rapidly, it appears that the transition of CO_2 from supercritical fluid to gas triggers an oscillation of fluid-filled cavities and fractures very close to the wellbores in which the monitoring arrays were deployed. In many aspects, the observed waveforms show a striking similarity to those modeled for degassing processes below volcanoes. We suggest that the single force represents bubble growth and resulting oscillations in cement cavities between the steel casing of the well and the rock adjacent to the wellbores and/or within fractures in the rock just outside the wellbores.

Citation: Bohnhoff, M., and M. D. Zoback (2010), Oscillation of fluid-filled cracks triggered by degassing of CO_2 due to leakage along wellbores, *J. Geophys. Res.*, *115*, B11305, doi:10.1029/2010JB000848.

1. Introduction

[2] Carbon capture and storage (CCS) is becoming an increasingly important technology to stabilize CO_2 contents in the atmosphere [e.g., *Intergovernmental Panel on Climate Change* (*IPCC*), 2007; *Schrag*, 2007]. CCS entails CO_2 capture from large industrial processes, mainly power generation from fossil fuels, and injection into deep geological formations. Geological formations of interest include depleted oil and gas reservoirs, deep saline aquifers and unminable coal beds. One principal requirement for CCS is to confine the CO_2 from leakage to other strata, shallow potable groundwater, or to the atmosphere over long time periods [e.g., *Bachu*, 2008]. It is therefore critically important to establish monitoring techniques to detect potential leakage and understand the related physical processes during and after sequestration of CO_2.

[3] At typical temperature and pressure conditions in the shallow crust, CO_2 is buoyant in most subsurface environments [*Pruess*, 2008]. Three main potential pathways for CO_2 to leak from its targeted storage formation have been recognized [*Espie*, 2004]: Leakage through the caprock, migration along preexisting subvertical faults or fracture zones or escape along/through wells that may have poorly cemented well casings [*Celia et al.*, 2004; *Bachu et al.*, 2004; *Duguid et al.*, 2004]. Obviously, well-cemented casing is needed to prevent vertical migration along wells penetrating the formations being used for sequestration [*Bachu and Bennion*, 2009]. CO_2 is notorious for washing out cement and corroding metal pipes [*Powers*, 2006] and leakage of sequestered CO_2 along wellbores, in particular behind the casing (where it cannot be directly traced), has been recognized as one of the biggest challenges in CO_2 sequestration [e.g., *Bachu et al.*, 2004]. With more than a million wellbores on the North American continent (the great majority of which are in oil and gas reservoirs) which could be considered for CCS [*IPCC*, 2007], this clearly becomes an important issue related to ensuring long-term storage of CO_2 in the subsurface.

[4] In gas storage projects, periodic acoustic well logs are run to detect enhanced acoustic noise levels to search for behind-casing gas flow in the well [*Smolen*, 1995]. *Bakulin and Korneev* [2008] report detection of tube waves in shallow wells which they attribute to vertical gas migration in a deeper well nearby. In this study we present evidence of a different type of seismological phenomenon, impulsive microseismic events that appear to result from oscillation of fluid-filled cracks triggered by degassing CO_2 close to monitoring wellbores where seismic arrays were deployed during a CO_2 injection with downhole Passive Seismic Monitoring (PSM) experiment. PSM is a well-known technique commonly used in different environments, usually with one or more arrays of downhole

[1]Department of Geophysics, Stanford University, Stanford, California, USA.
[2]Now at Helmholtz Centre Potsdam, GFZ German Research Centre for Geosciences, Potsdam, Germany.

0148-0227/10/2010JB000848

seismometers, to detect microearthquakes associated with hydraulic stimulation of hydrocarbon and geothermal reservoirs (see recent reviews by *Shapiro* [2008] and *Bohnhoff et al.* [2010a]). Our study is part of a pilot CO_2 injection experiment in the Michigan Basin where CO_2 was injected into a saline aquifer. Some 10,000 tons of supercritical CO_2 were injected at 1050 m depth into the Bass Island Dolomite (BILD), utilizing CO_2 that had been used for enhanced oil recovery (EOR) into the Coral Reef reservoir at ~1670 m depth for several years (see Figure 1a). The BILD Formation is a porous dolostone at the top of the Silurian Bass Islands group which is found throughout the Michigan Basin at an average thickness of 15 m. Its local thickness is 22 m at an average porosity of 13% and an average permeability of 22 mdarcy. The Bois Blanc Formation is overlying the BILD Formation and described as a cherty carbonate strata of 78 m thickness (Figure 1a). Although it could locally be considered as a seal due to the apparent lack of suitable injectivity potential, it has been mentioned in other parts of the Michigan Basin as another potential storage target. The primary caprock is the Amherstburg-Lucas Formation, a dense limestone with very low porosity. Permeability measurements showed very low permeability, mostly less than 1 mdarcy [*Barnes et al.*, 2008].

[5] A description of our combined CO_2 sequestration and PSM experiment is given by *Bohnhoff et al.* [2010b]. In that it was concluded that the observed microseismic events are associated with leaking CO_2 rising from the Coral Reef Formation along the annulus of the two monitoring wellbores. The unusual microseismic events occurred only during injection into the deeper Coral Reef Formation for enhanced oil recovery (EOR), not when injection was occurring into the BILD Formation, and they only occurred close to the monitoring seismic arrays, hundreds of meters from where the BILD injection was occurring. In this paper we examine the seismological character of these unusual events and discuss possible source processes.

[6] A total of 225 induced microseismic events were detected by the two downhole seismic arrays deployed at 900–1000 m depth (Figure 1b). Only a single microearthquake was strong enough to be detected on both sensor arrays. As discussed by *Bohnhoff et al.* [2010b], it was also the only event representing a typical shear slip source process as usually observed for induced microearthquakes [e.g., *Rutledge et al.*, 1994; *Shapiro*, 2008]. All other events were strong enough to generate prominent waveforms at one of the arrays but too weak to be seen on the other. 201 events were detected at the eastern array and 23 were detected on the western array (Figure 1b).

[7] Hypocenters were determined by applying a least squares inversion to the P wave arrival times at the individual sensors of the arrays. A homogeneous velocity model with v_p = 4.8 km/s was used and the position of the sensor with the earliest arrival time served as the starting location for the inversion. As only P wave arrival times (but no shear wave arrival times) were inverted no information on sensor-specific source distances was available and particle motion could not be used since a substantial number of the sensors were located in the seismic near field (see below). Therefore, the actual inversion is performed in 2D and the obtained hypocenters contain information about depth and lateral distance to the array, but there is no information about the azimuthal position. In addition, a total of 40 events produced clear P onsets on the sensors but occurred above or below the arrays not permitting us to determine their exact source location. However, the rapid decay of P wave amplitudes across the array indicates that these events have occurred in very close vicinity to the arrays. These events are summarized and indicated by the open circles in Figure 1b. For 94 events, we obtained stable hypocenter locations, all of which are in direct vicinity of the seismic array they were detected on. The hypocentral distance of the nearest sensor was typically less than 10 m (Figure 1b).

[8] The microseismic events have unusual waveforms and we classify them into six categories, principally on the basis of their spectral characteristics (Table 1 and the auxiliary material): A-type events have relatively high frequency contents, typically between 100 and 500 Hz, although frequencies as high as 1000 Hz are sometimes observed (Figures 2a and 2b).[1] In contrast, B-type events have relatively lower frequencies, typically between 40 and 150 Hz (Figures 2c and 2d). B-type events generally have larger amplitudes than A-type events and are sometimes clipped on the sensors nearest to the source. C-type events contain both the frequency ranges of type-A and −B events in varying proportions (Figures 2e and 2f). As described below, all events of types A–C are interpreted to represent the same general source process. Some of the type A–C events have clear low-frequency, low-amplitude precursor signals (Figure 2g). A common characteristic of all of the microseismic events detected is that the events have either no shear waves, or extremely weak shear waves. Figure 2h shows one of the few events with shear waves. A number of event groups with highly similar waveforms within short time intervals (typically minutes to hours) are referred to as type D in Table 1. Most of these events are typically very weak and detected on too few sensors to allow us to reliably determine their hypocenters. The remaining 50 events (type E) were also very weak and too weak to be analyzed. For completeness, the single microearthquake event mentioned above is indicated as a type F event in Table 1.

[9] In Figure 3 we show the frequency spectrum for representative events of types A–C. Spectra from all sensors of one event were plotted. The heavy black line indicates the average spectrum from all of the sensors while the dotted lines represent individual sensors. All traces are normalized to their maximum. The frequency spectra of all events of type A–C are included in the auxiliary material.

2. Waveforms Characteristics

[10] In the following, we focus on event types A–C. All these events have consistent first arrivals with a phase velocity of 4.8 ± 0.2 km/s across the arrays (Figure 4a), but different dominant frequencies as described above. As this is the compressional wave velocity of the surrounding rock formation, these first arrivals are interpreted to be P waves and provide evidence that the events are located very close to the wellbores [*Bohnhoff et al.*, 2010b]. Because the phase velocity rapidly increases for hypocenters laterally offset from the array, an offset of 10, 20 or 50 m from the seis-

[1] Auxiliary materials are available in the HTML. doi:10.1029/2010JB000848.

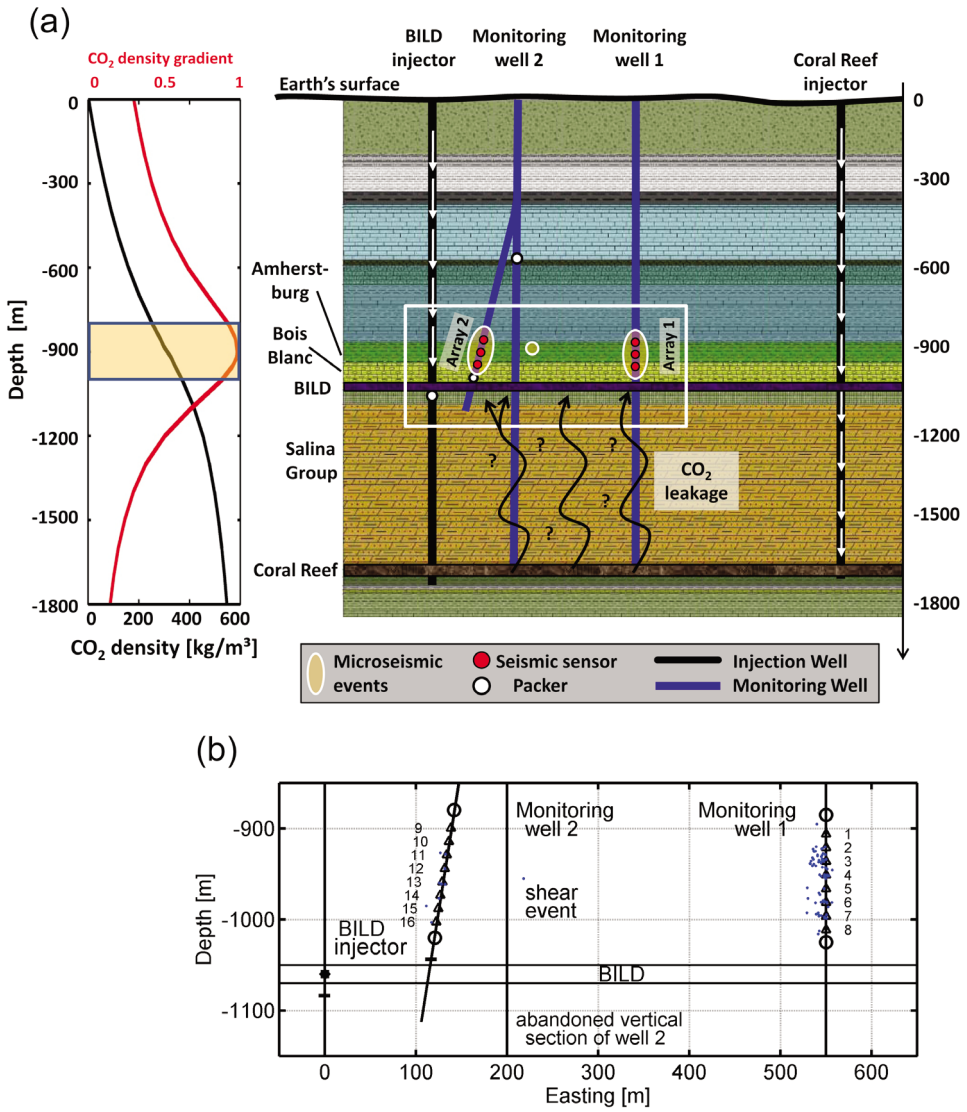

Figure 1. (a) (right) Conceptual model for CO_2 leakage identified by induced microseismicity occurring during rise from the Coral Reef reservoir along the annulus of two monitoring wells that each were equipped with a geophone array consisting of eight three-component sensors [after *Bohnhoff et al.*, 2010b]. The microseismic activity (indicated by the white ellipses) occurred only during CO_2 injection into the Coral Reef Formation through the injector well to the right while no such activity was observed during CO_2 injection into the Bass Island Dolomite (BILD) Formation except for a single seismic event observed above BILD (indicated by the white circle). That single event was also the only shear event and the only event seen at both sensor arrays. All events related to the Coral Reef injection were located in direct vicinity of the sensor arrays which is also the depth where the transition of CO_2 from supercritical to gaseous occurs based on local temperature (2.9°C/100 m) and pressure (hydrostatic) conditions and (left) applying the Peng-Robinson equation of state (PREOS). The white rectangle marks the area enlarged in Figure 1b. (b) Enlarged part of Figure 1a focusing on the two downhole seismic sensor arrays and the BILD injection well. The eastern monitoring well is vertical, while the western monitoring well consists of an older abandoned vertical part and a new part (in which the sensors were deployed) that is deviated toward the WNW. The small dots represent hypocenters of the locatable microseismic events (94 in total). In addition, the open circles above and below the sensor arrays represent a total of 40 events that could not be located precisely but that are known to be located close to either end of one of the arrays (see text for details). The only event seen on both sensor arrays was also the only shear event and is indicated. Black bars represent bridge plugs (packers).

Table 1. Overview on the Different Event Types Observed During Passive Seismic Monitoring of CO_2 Sequestration[a]

Event Category	Number of Events	Dominant Frequency (Range) (Hz)
A	15	~500 (300–1000)
B	33	~100 (40–150)
C	59	both dominant frequencies ranges of A and B type
D	68	similar but too weak events
E	50	too weak
F	1	~500 (P), ~150 (S)

[a]See text for details.

mometer at the end of an array would result in a phase velocity of 5.3, 5.8 or 7.6 km/s, respectively, clearly much higher than the formation velocity. The theoretical curve for the phase velocity of compressional waves with increasing lateral offset from a vertical sensor array is shown in Figure 4c. Furthermore, the observed phase velocity confirms that the events did not occur within the wells. A direct arrival traveling along the wellbore would have a first arrival associated with a wave traveling along the steel casing with a phase velocity > 6 km/s, whereas waves traveling within the wellbore (tube waves) would have a phase velocity of approximately 1.5 km/s [e.g., *White*, 1983; *Paillet and Cheng*, 1991]. In fact, a clear second arrival was seen in 44 events with consistent phase velocities of 1.6 ± 0.1 km/s across the array (Figure 4b) and are thus identified as tube waves (see Figures 2a, 2b, 2e, and 2h). Tube waves can be generated when P waves enter the wellbore due to the density contrast between the rock formation/cement to steel casing/sensor array [*White*, 1983; *Paillet and Cheng*, 1991]. Tube waves are sometimes reflected at ends of the seismometer arrays due to the density contrast between the wellbore with and without the sensor array within it (Figures 2a and 2e). The observed value of 1.6 km/s is valid only in the high-frequency limit since the tube wave is dispersive with velocity that decreases with increasing wavelength [*Biot*, 1952].

[11] Overall, we note that the observed P waves are by far more energetic than expected for a typical shear source process and that only a small number of S phases were observed that were all weak in amplitude. The near complete absence of shear waves in these events is not what would be expected for microseismic events caused by slip on faults. The shear waves associated with such events are expected to have substantially higher amplitudes than the compressional waves in the seismic far field for a double-couple source process [e.g., *Aki and Richards*, 2002]. For an event near the end of one of the 105 m long seismometer arrays, shear waves would be expected to arrive ~0.02 s after the P waves at the most distant sensor assuming $v_p/v_s \approx 1.9$. Thus, they should be clearly identifiable on the seismograms although there might exist some weak S phases that are hidden in the coda of the larger-amplitude P waves for events occurring within the arrays.

[12] In Figure 5 we show all of the P wave polarities classified by the event type. We subdivide the events with respect to their respective hypocentral locations to the sensor array (above, below or within). Note that for almost all events we observe a uniform polarity pattern for each event. That is, either all sensors indicate upward or downward motion regardless of where the event is located with respect to the individual sensors. Note that sensors 1 and 9 are the shallowest (8 and 16 are the deepest) in the eastern and western monitoring wells, respectively. Moreover, we observe a comparable number of events with upward (~50 events) and downward (~35 events) first motion polarities. As most of the events occurred within the depth extent of the sensor arrays, we conclude that the source of these events cannot be a simple isotropic point source as such a source would result in upward motion above the source and downward motion below the source (i.e., first motions would always point away from the isotropic source). In section 3, we examine both a double-couple source process (appropriate for shear on faults) and a single force source that might be caused by expansion of a planar fracture during degassing processes, e.g., below volcanoes, or during landslides or mine collapses [e.g., *Weichert et al.*, 1994; *Nishimura*, 1998].

[13] To further investigate the source process of these unusual microseismic events, we examine the rate at which the P wave amplitudes decay across the arrays. As mentioned above, all of these unusual microseismic events are

Figure 2. Examples for the different waveform characteristics obtained during the CO_2 injection experiment. For each event the vertical components of the eight sensors from the relevant seismic array are shown (array 1, sensors 1–8; array 2, sensors 9–16; see Figure 1 for location of sensor arrays). All seismograms are filtered with a Notch filter to eliminate 60 Hz and multiples as well as individual ringing signals of the sensors. (a) Type-A event observed at array 2 with dominantly higher-frequency contents of the P wave (~600–900 Hz) and clear tube waves that are generated at the upper end of the sensor array when the P wave enters the monitoring well. The source is located slightly above the array. Later in the seismogram a tube wave reflected at the lower end of the sensor array is seen then propagating upward. (b) Type-A event similar to the one in Figure 2a but with a hypocenter that is located within the depth extent of the array close to sensor 11. (c) Type-B event observed at array 1 with dominantly lower-frequency contents of the P wave (~100 Hz), although some higher frequencies can be seen on top of that. The event is located close to sensor 4. (d) Type-B event similar to the one in Figure 2c with slightly lower (~80 Hz) dominant frequency contents. The event occurred close to sensor 3. (e) Type-C event observed at array 2 with both higher- and lower-frequency contents (predominantly seen at sensor 12 that is closest to the source). As for most events a clear tube wave but no S phase is seen in the waveforms. (f) Type-C event with comparable contributions of lower- and higher-frequency contents on all sensors of array 1. The event is located close to sensor 4. (g) Type-A event observed at array 1 with dominantly higher-frequency contents and a clear precursor phase at constant time offset prior to the P wave at all sensors. (h) Type-C event observed at array 1. This event of one the few with a weak but notable S phase. The source is located close to sensor 7. This event (72) is also indicated in Figure 7c as it represents one of the events with higher S to P amplitude ratios.

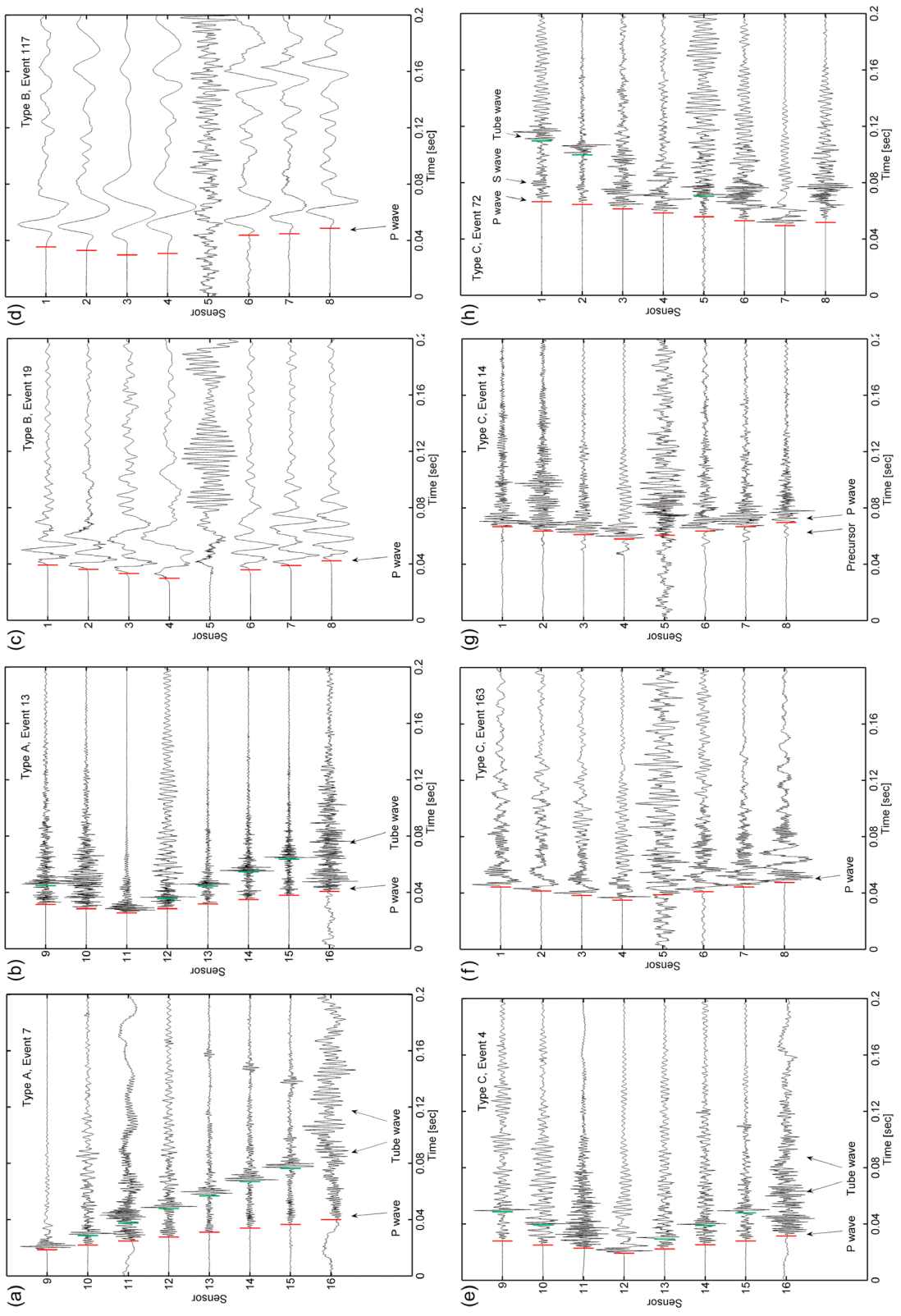
(a)
Type A, Event 7
P wave
Tube wave
(b)
Type A, Event 13
P wave
Tube wave
(c)
Type B, Event 19
P wave
(d)
Type B, Event 117
P wave
(e)
Type C, Event 4
P wave
Tube wave
(f)
Type C, Event 163
P wave
(g)
Type C, Event 14
Precursor
P wave
(h)
Type C, Event 72
P wave
S wave
Tube wave
Sensor
Time [sec]

Figure 2

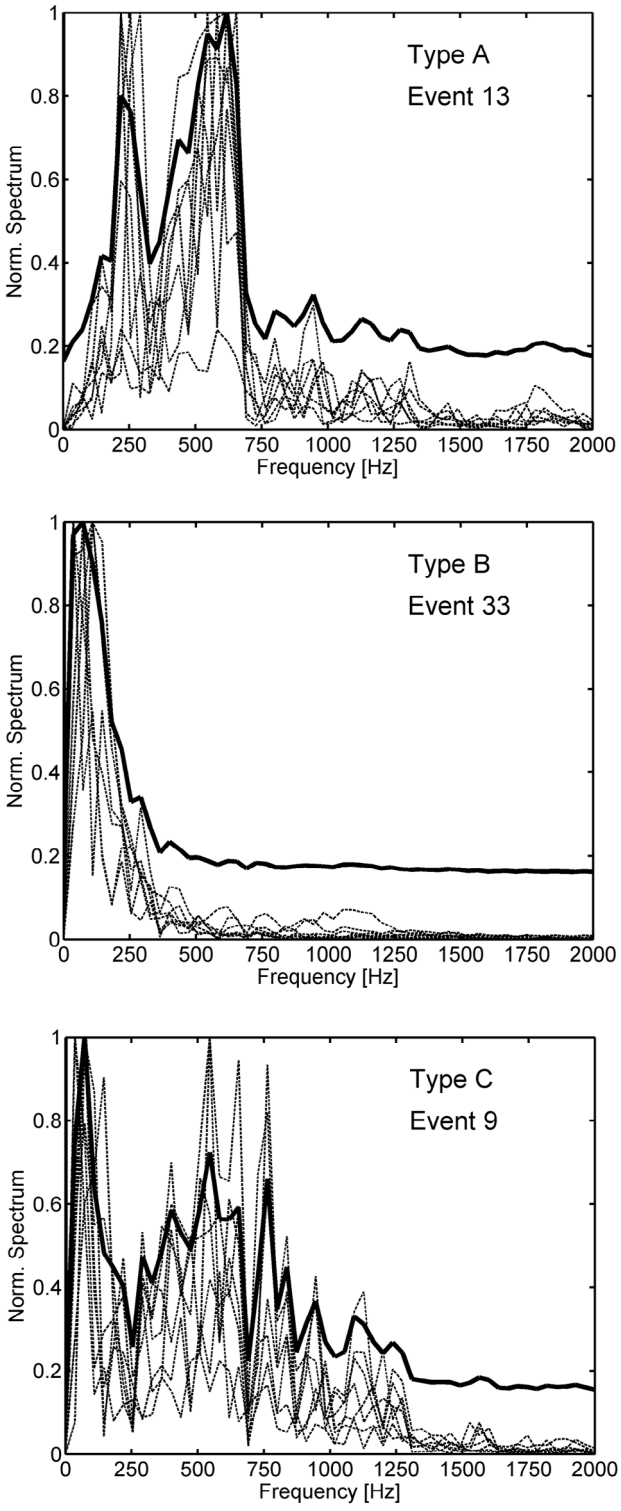

Figure 3. Frequency spectrum for representative events of type A, with dominantly higher-frequency contents; type B, with dominantly lower-frequency contents; and type C with comparable contributions from both dominant frequency ranges. Dotted lines show spectra of individual sensors of the respective array, while the heavy lines indicate the average spectrum from all sensors. All traces are normalized to their maximum. Frequency spectra for all events of types A–C are shown in the auxiliary material.

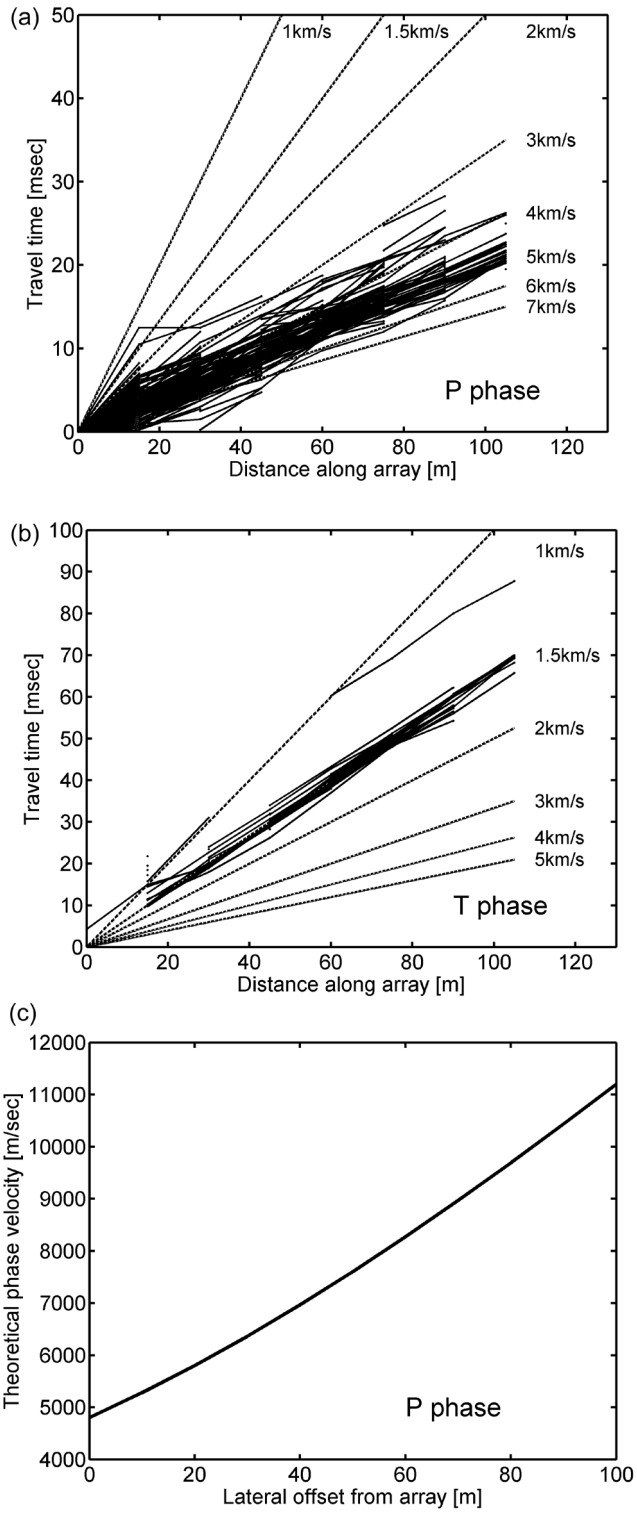

Figure 4. Phase velocities determined from travel times across the sensor arrays for (a) P waves and (b) tube waves. While P waves give a stable 4.8 ± 0.2 km/s representing an integral velocity from the formation around the monitoring wells, the tube waves give 1.6 ± 0.1 km/s representing the acoustic velocity of the borehole fluid. (c) Theoretical phase velocity for P waves with lateral distance from the sensor array for a formation velocity of 4.8 km/s.

seen on only one of the arrays and not the other, indicating that the energy released in each event is quite small. Theoretical approaches describing the Green's function of different types of source processes involving P and S phases typically separate the seismic wavefield into the near field and far field [e.g., *Aki and Richards*, 2002]. Near field behavior should describe the seismic waves within a couple of wavelengths of the source while the far field describes waveform characteristics at greater distances. In our case, with dominant frequencies of ~500 Hz and V_p = 4.8 km/s, the seismic near field should extend to distances of about 20–30 m from the source. Given a receiver spacing of 15 m in our case, the one or two sensors closest to the source would often be located in the seismic near field.

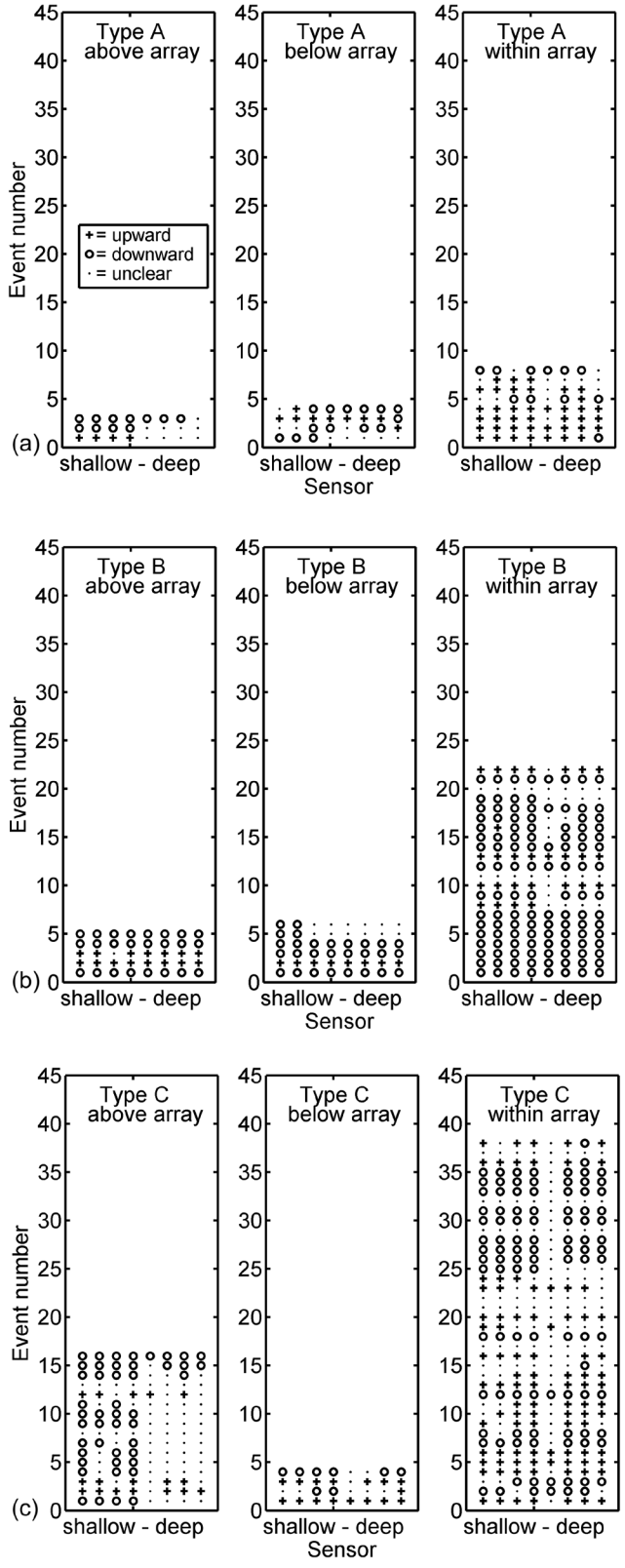

Figure 5. Observed polarities of the P phase onsets for event types A–C. For each type the events are further subdivided into events occurring above, below, and within the relevant sensor array. A "plus" indicates upward motion, and a "circle" indicates downward motion. A "dot" means no polarity could be determined. Sensors 1 and 9 are the shallowest, while sensors 8 and 16 are the deepest sensors of the arrays, respectively. For almost all events we observe a uniform polarity pattern no matter where the event is located with respect to the sensor array. About 50 events have uniform upward motion, and ~35 events have uniform downward motion.

[14] In the seismic far field the amplitude decay of the elastic waves decreases with 1/r (where r is the hypocentral distance in m) due to geometrical spreading while the amplitude decay is $1/r^2 - 1/r^4$ in the seismic near field [*Aki and Richards*, 2002]. Also, the 3D particle motion is linear in the seismic far field while it is highly nonlinear in the seismic near field [e.g., *Vavryčuk*, 1992, 1994]. Analysis of particle motion for the obtained P waves indeed shows a nonlinear pattern for the majority of the obtained waveforms, especially at those sensors closest to the source. As a result, we cannot use the 3D particle motion of the P onset as additional parameter to further refine the hypocenter precision. However, we note that recordings of all seven calibration shots conducted after the deployment of the geophones and prior to the onset of the CO_2 injection into the BILD Formation resulted in linear particle motions at the sensors allowing to determine the orientation of the individual geophones at depth (see *Bohnhoff et al.* [2010b] for details). To quantify whether our near-source recordings were in fact obtained in the seismic near field we systematically determine the amplitude decay across the respective sensor arrays. This is a good first-order approximation to hypocentral distance as the lateral offsets between hypocenter and sensor array is typically <10 m. We calculate the maximum 3D particle motion of the P phase at each sensor within a time window of $\Delta t = 5\ ms + 0.2\ ms/m \times r$ (where r is in m) after the P onset. We then normalize the amplitudes of all sensors to the maximum amplitude for that event (which was obtained at the sensor nearest to the source) and plot the amplitude decay across the array (Figure 6). The dotted lines in Figure 6 represent different amplitude decay rates ($1/r$, $1/r^2$, $1/r^3$ and $1/r^4$, from top to bottom). We plotted the amplitude decay separately for type A–C events (Figure 6). A few events have clipped signals at one or more sensors nearest to the source which are not plotted. Note that we obtain a uniform strong decay of the P wave amplitudes ($1/r^2 - 1/r^4$) with source distance indicating that the sensors nearest to the source are indeed located in the seismic near

field. At greater hypocentral distances the amplitude decay approaches 1/r as expected for the seismic far field.

[15] In contrast to the rapid P waves the amplitude decay for the tube waves is relatively small (see Figures 2a and 2b). This observation correlates well with our understanding that tube waves generally show little energy loss as they are trapped within the borehole [*Paillet and Cheng*, 1991].

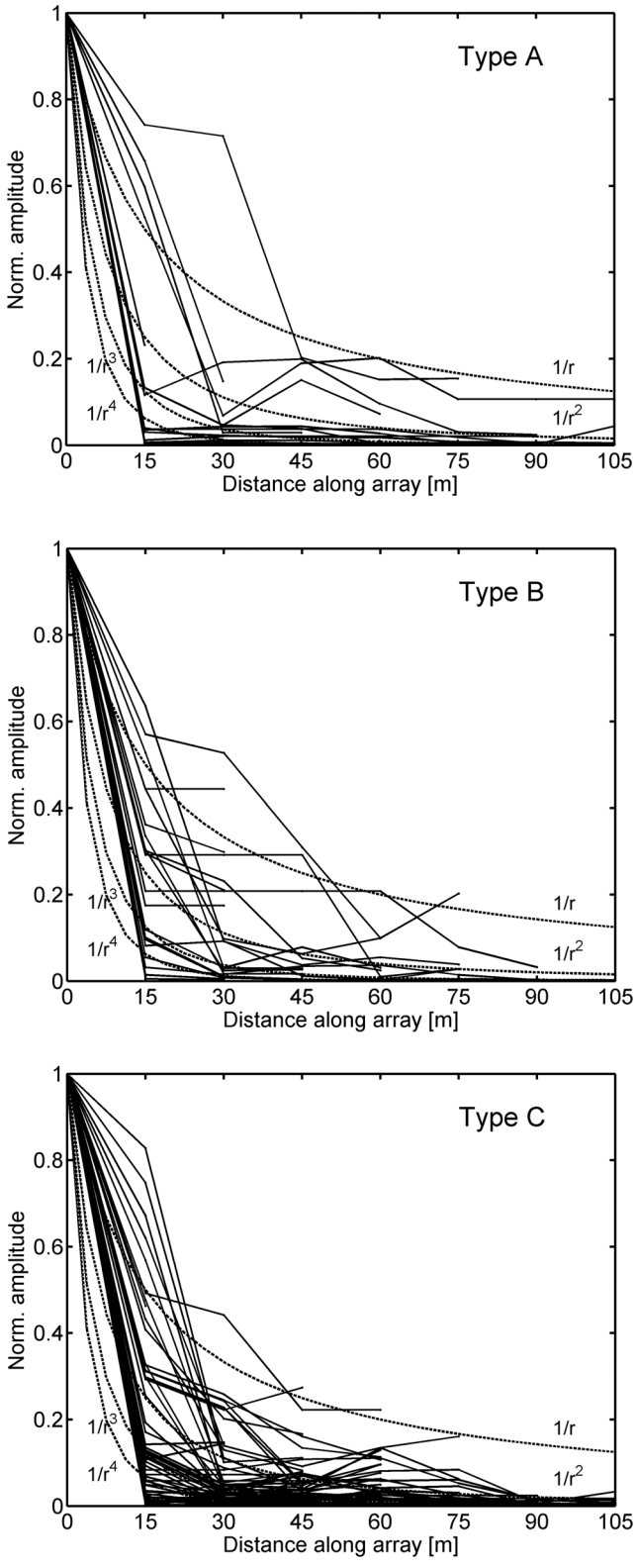

[16] In Figure 7 we show the theoretical radiation pattern (Figure 7a) and theoretical values of S to P amplitude ratios with takeoff angle (at two scales) for a double couple (Figure 7b) as well as a single force (Figure 7c) source following *Udias* [1999], *Shearer* [1999], and *Aki and Richards* [2002]. Furthermore, we show the radiation pattern for an isotropic source (but not S to P ratios since no S waves are generated). The principal observation is that the ratios of S to P are expected to be high for small takeoff angles in the case of a double-couple source but low in the case of a single force source process (see Figures 7b and 7c, respectively). In Figure 8 we show observed S to P wave amplitude ratios with takeoff angle from the source for the events of types A–C. For the P waves we use the same time window described above. Because no S onset times are available, the time and window lengths for the S waves was calculated based on the theoretical S-P differential travel time. We calculate the maximum 3D particle motion within the P and S phase windows and plot the S to P amplitude ratios with takeoff angle for each event. Crosses in Figure 8 represent sensors located in the seismic far field in order to compare them to the far-field theoretical variation of S to P amplitudes. The signal-to-noise ratios for the observed P waves are typically 3–5 in the seismic far field. This is substantially reduced compared to those in the seismic near field. The obtained S to P amplitude ratios are generally smaller than expected for high signal-to-noise ratios. The theoretical lines (dotted) on Figure 8 are those shown in Figure 7. As all events occur very close to the arrays, the distant sensors all have very low takeoff angles. At the same time the location precision of ~5 m results in a less precise determination of the sensor-specific takeoff angle near the source (approximately ±10°). As described earlier, 40 events occurred slightly above or below the array which could not be located accurately. In order to use those events for the analysis of amplitude ratios (most have acceptable signal-to-noise ratios) we fixed their hypocenters to 5 m off the borehole at the depth of the shallowest and deepest sensor, respectively. While this assumption may be incorrect, the majority of sensors have extremely low takeoff angles for these events and the exact distance of the event from the borehole is relatively unimportant.

[17] While there is a great deal of scatter in these observations, at low takeoff angles we coherently observe

Figure 6. Observed amplitude decay for P waves across the sensor arrays for all events of type A, type B, and type C. The horizontal axis shows meter along the sensor array which is identical to hypocentral distance in first-order approximation due to lateral offsets between hypocenter and sensor array of typically <10 m. The vertical axis shows the amplitude at each sensor with normalized to the amplitude of the sensor nearest to the source. Hyperbolas represent different amplitude decay rates ($1/r$, $1/r^2$, $1/r^3$, $1/r^4$ from top to bottom). Events with clipped amplitudes were excluded. Amplitudes were calculated as maximum elongation from the 3D particle motion of the P onset at each sensor within a time window of $\Delta t = 5$ ms + 0.2 ms/m × r (r = hypocentral distance in m).

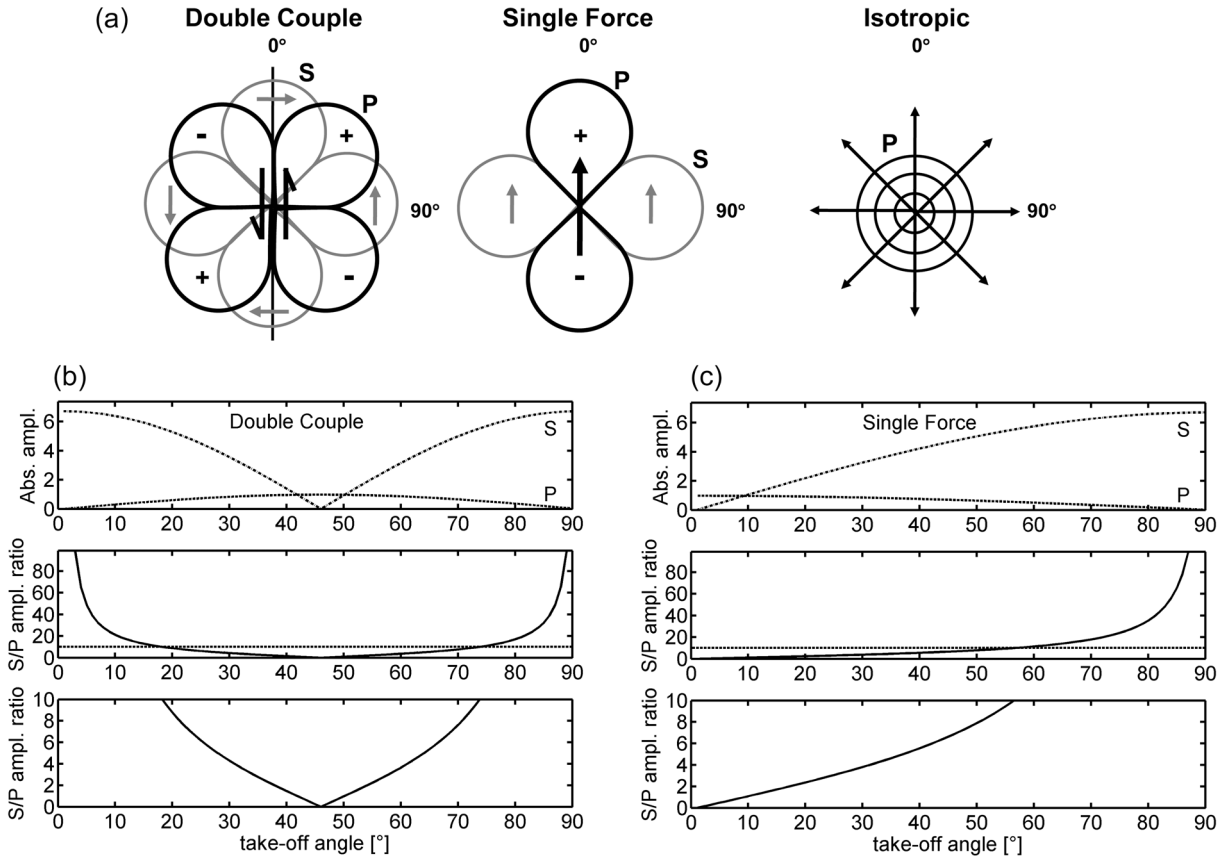

Figure 7. (a) Far-field radiation pattern for a double couple, a single force, and an isotropic source process radiation pattern (black, P waves; gray, S waves) [see, e.g., *Udias*, 1999; *Shearer*, 1999; *Aki and Richards*, 2002]. The arrows indicate the direction of first motion. The takeoff angle is measured from vertical up (or down, respectively) toward horizontal. For Figure 7a to be at true scale, the shear wave pattern should be enlarged by a factor of $(v_p/v_s)^3$. (b) S to P amplitudes and their ratios for a double-couple source process: (top) Theoretical amplitudes with takeoff angle for P and S waves following *Aki and Richards* [2002] assuming v_p = 4.8 km/s, v_p/v_s = 1.9, ρ = 2.3 g/cm^3. (middle) Resulting S to P amplitude ratios (bold line). The dotted line marks the S to P amplitude ratio = 10 as the upper boundary of the enlarged part in the bottom figure. (bottom) Enlargement of S to P amplitude ratio 0–10 to facilitate comparison with observed values as in Figure 8). (c) Same as in Figure 7b but for a single force source process.

S to P amplitude ratios up to ~4 for all events (Figure 8). As can be seen in Figure 8, the observed S to P amplitude ratios clearly point toward a dominant single force source process. This said, note that a small number of events have relatively high S to P amplitude ratios at low takeoff angles which might indicate a minor double-couple component included in addition to the dominant single force. As an example we highlighted the values for the sensors of event 72 in Figure 8c and refer to the waveforms of this event which are shown in Figure 2h. In summary, based on the results from the observed S to P amplitude ratios we conclude that the dominant source process for the observed microseismic events is neither a double-couple or isotropic point source but rather a single force.

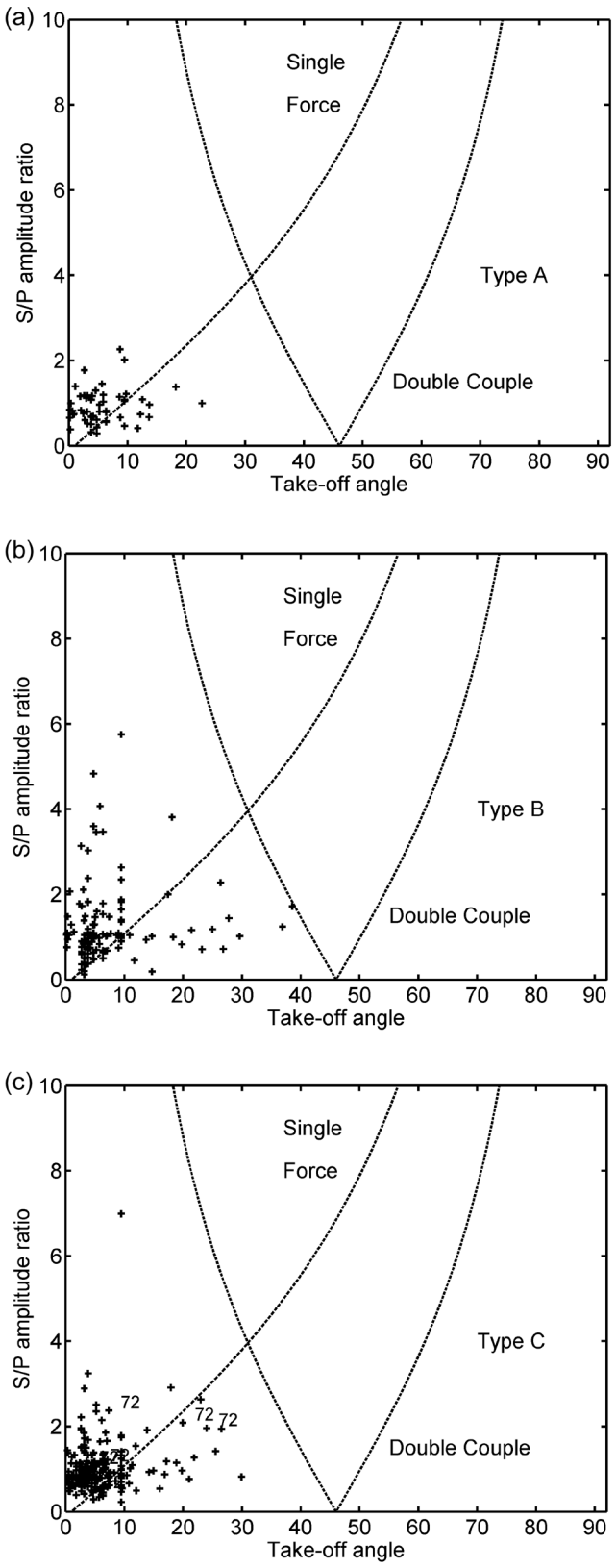

Figure 8. Observed S to P wave amplitude ratios for all events of (a) type A, (b) type B, and (c) type C plotted with takeoff angle from the source. The takeoff angle is measured against vertical up and vertical down, respectively, and therefore covers the interval 0°–90°. Since all events occur very close to one array, the majority of sensors are located at low takeoff angles. Amplitudes were calculated from the maximum particle motion within a time window for P and S waves based on P picks and the S-P times calculated from the individual source-receiver geometry. Only sensors with signal-to-noise ratios for P > 4 are plotted. The events producing higher S to P wave ratios are those where weak S phases were identified in the seismograms. Event 72 is indicated as an example for comparatively large S amplitudes in Figure 8c, and the waveform for this event is shown in Figure 2h. Theoretical curves for S to P amplitudes ratios for a double couple and single force source process are plotted as dotted lines (see also Figure 7).

3. Discussion and Conclusion

[18] Long-term passive seismic monitoring (PSM) of microseismic events has not yet been systematically investigated as a monitoring technique to monitor potential behind-casing flow of sequestered CO_2. There is a striking difference between the noise monitoring technique mentioned in the Introduction and the distinct microseismic events presented in this study. Because the volume expansion of the CO_2 during degassing appears to be the triggering source for the events, in any given monitoring study this would occur at a distinct depth interval that depends on the local temperature and pressure conditions. This requires systematically placing sensors in monitoring wells at the appropriate depths [*Bohnhoff et al.*, 2010b] to detect potential leakage from storage reservoirs. In the following we further elaborate on the underlying seismic source processes of these events.

[19] In addition to the three possible source mechanisms for the observed seismic signals that we considered (a double couple, a single force and an isotropic source) we can also relate our observations to an opening tensile crack as potential source. While a subvertical crack would satisfy the amplitude ratios observed in our study (far field radial displacements are presented by *Chouet* [1988]), such a source would not be consistent with the observations that first motion polarities are the same for all sensors for a given event.

[20] From the observed first-motion polarity pattern and the presence of a small amount of shear wave energy in many sources, we exclude an isotropic source as a potential dominant source mechanism. Instead, most evidence points to a single force mechanism rather than the expected dou-

Table 2. Summary of Observations Constraining the Potential Source Process Underlying the Observed Seismic Signatures[a]

Source Type	Consistent With Polarity Pattern?	Consistent With S to P Amplitude Ratio?
Isotropic	No	Yes
Double couple	Yes	No
Tensile crack	No	Yes
Single force	Yes	Yes

[a]See text for details.

ble-couple mechanism for injection-induced seismicity associated with slip on faults (Table 2).

[21] As mentioned above, the CO_2 was injected in supercritical status and the microseismicity occurred only during injection into the Coral Reef, when the reservoir pressure was relatively high. During its rise along the wellbores, the CO_2 undergoes a transition from supercritical to gaseous due to decreasing temperature and pressure. The volume increase of the CO_2while rising is most rapid in direct vicinity of the seismic sensors at ~800–950 m depth (Figure 1a, left) which is also the depth at which these unusual microseismic events were detected (Figure 1b). As discussed by *Bohnhoff et al.* [2010b], such degassing processes are accompanied by a dramatic volume expansion of the CO_2 which is capable of generating a local pressure pulses when pressure changes rapidly as the CO_2 squirts through fluid-filled cement cavities, and preexisting fractures near the wellbore. We suggest that such pressure pulses serve as the trigger initiating oscillations in the cement cavities, and preexisting fractures thereby generating elastic waves. In combination, both, the pressure pulse caused by CO_2 expansion and the oscillation of the resonators are believed to be the sources for the observed P wave pattern producing the observed events of types A–C. Regarding the distinct observed dominant frequencies it remains unclear whether either type of frequency (40–150 Hz for type B events, 300–1000 Hz for type A events) can be directly related to the bubble expansion or the oscillation, respectively. However, since we expect the bubbles to have varying sizes that expand in fluid-filled fractures and cavities of different size we assume that it is not possible to clearly associate either dominant frequency with the bubble expansion or triggered oscillation, respectively, based on the obtained waveforms and source-receiver geometry. While we classified three types of events with relatively high (type A), relatively low (type B) or both (type C) frequency contents, we note that there are a number of events of type A and B containing also minor portions of lower and higher frequencies, respectively. We therefore conclude that all three types do represent the same type of source process (the combined bubble expansion plus subsequent oscillation of fluid-filled fractures) while the portion of either frequency range varies and is defined by the local conditions at the source [see also *Chouet et al.*, 2006; *Shimomura et al.*, 2006]. A single force implies mass advection. Such mass advection, however, requires an accompanying volumetric source which in our case is the transient pressure disturbance due to elastic deformation of the cavities through which mass is suddenly moving. In this whole interaction of pressure pulses induced by the injection into the Coral Reef Formation also pressure diffusion might be a considerable effect involving the theory of poroelasticity [*Biot*, 1956]. In order to estimate the expected source dimension of the resonators in our case ~ 0.1–1 m seems to be a realistic range when downscaling theoretical attempts by *Chouet* [1988] relating emitted frequencies to source dimensions.

[22] These arguments are strengthened by the fact that our observed waveforms (especially type C events with both dominant frequency ranges) are similar to synthetic seismograms computed for volcano-related degassing processes [*Chouet*, 1988, Figure 7]. Studies on physical processes acting in magma chambers and dikes below volcanoes during degassing of rising CO_2 date back to the 1970s [e.g., *Blackburn et al.*, 1976] describing explosive sources as the dominant mechanisms during rise and formation of gas bubbles. The explosions were associated with bursting of large bubbles at the magma surface while the gas segregation starts at considerable depth and bubble size increases during rise. In later studies by *Chouet* [1988] and *Chouet et al.* [2006], theoretical models on the dynamics of gas exsolution, bubble expansion and associated crack response were proposed and further refined involving a step drop in pressure, which induces gas exsolution and bubble expansion resulting in a volumetric expansion of the crack. They note that their source shows many narrow-band spectral peaks that characterize the interaction of the various modes of resonance of the crack. Indeed we also observe distinct peaks in the frequency spectra of the seismograms as discussed above (see also frequency spectra in the auxiliary material). In summary we note a striking similarity of the here presented recorded seismograms recorded in the field and the synthetic seismograms modeled for the oscillation of fluid-filled cracks in magmatic systems. The processes discussed here as "degassing signals" below volcanoes may as well be part of what is commonly referred to as volcanic tremor. Especially the much lower frequency of tremor may have to do with the fluid viscosity and length scale of the crack network. However, we note that the frequency range observed in our study is substantially higher than those of the signals commonly known as "volcanic tremor" reflecting processes, e.g., related to magma migration and covering frequencies as low as several Hz and below [e.g., *Riuscetti et al.*, 1977; *Julian*, 1994].

[23] If the degassing process occurs in a pure fluid environment, such as in a magma chamber below a volcano, it would form a purely isotropic source. Such source processes below volcanoes have been widely discussed in the literature (see above and, e.g., *Neuberg and Luckett* [1996]). In our case, the CO_2 rises from the Coral Reef reservoir toward the surface along the annulus of the monitoring wellbores following several possible pathways: material interfaces between rock formation and cement and/or cement and casing and/or cavities in the cementation of the wellbore annulus and/or permeable cracks and fractures within the rock formation in direct vicinity of the wellbore off the annulus (Figure 9a). As a result, we suggest that the degassing does not occur isotropically. Instead, the actual bubble expansion seems to occur subvertically along fractures and cement cavities as indicated by the uniform polarities at the sensors indicating both upward or downward first motion (Figure 9b). Cement cavities and fractures are presumably subvertical as they otherwise would not represent potential pathways for upward migration of CO_2. The seismic waves resulting from

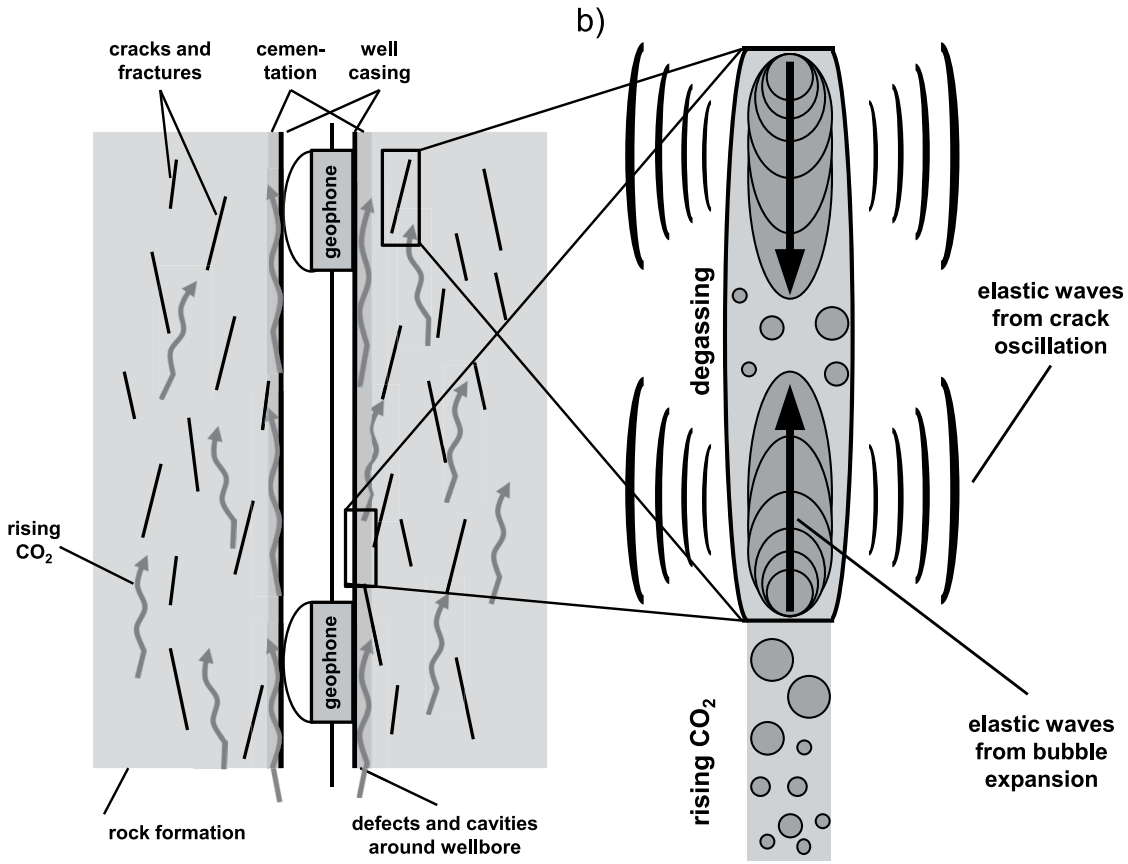

Figure 9. Sketch of the observed seismic source process generated during transition of CO_2 from supercritical to gaseous while rising from its storage reservoir along and around preexisting wellbores. (a) Bold black lines indicate small-scale fractures around the wellbore within the rock formation. The rising CO_2 is indicated by curved arrows. Black rectangles are selected representative areas enlarged in Figure 9b where degassing results in a single force source process generating elastic waves observed at the geophones. (b) Schematic bubble expansion and subsequent oscillation of a fluid-filled fracture/cement cavity. The bold arrow indicates the bubble expansion, and curved lines to either side mark propagating elastic waves from the oscillation.

the bubble expansion and subsequent oscillation of the resonators overall seem best represented by a single force mechanism as indicated by the observed polarity pattern and S to P amplitude ratios.

[24] For some events we observe a clear precursor phase (Figure 2g). These precursor phases have constant time offsets for all sensors of the respective event. Therefore, they are believed to be part of the same process as the "main event" which reflects the bubble growth during degassing. However, the precursor signals are nonuniform as they look different for each event. It is possible that these signals represent an early initiation phase of the bubble growth during volume expansion. In our seismic recordings precursory signals are observed for a small number of events indicating that they do not seem to be a general phenomenon in the observed source processes. The precursory phases might be generated only under rather specific local conditions.

[25] **Acknowledgments.** The data used in this study were acquired by the Engineering Seismology Group, Kingston, Ontario, Canada. We thank Neeraj Gupta and Jacqueline Gerst for useful discussions and for carrying out the PSM experiment. We thank William L. Ellsworth, Bernhard Chouet, Norm Sleep, and Jerry Harris for fruitful discussions. Constructive comments by the Associate Editor Robert L. Nowack, Don C. Lawton, and an anonymous reviewer helped to improve the manuscript. We are grateful to the Deutsche ForschungsGemeinschaft (DFG) for funding within the Heisenberg program.

References

Aki, K., and P. G. Richards (2002), *Quantitative Seismology*, 2nd ed., Univ. Sci. Books, Sausalito, Calif.

Bachu, S. (2008), CO_2 storage in geological media: Role, means, status and barriers to deployment, *Prog. Energy Combust. Sci.*, *34*, 254–273, doi:10.1016/j.pecs.2007.10.001.

Bachu, S., and D. B. Bennion (2009), Experimental assessment of brine and/or CO_2 leakage through well cements at reservoir conditions, *Int. J. Greenhouse Gas Control*, *3*, 494–501, doi:10.1016/j.ijggc.2008.11.002.

Bachu, S., J. M. Nordbotton, and M. A. Celia (2004), Evaluation of the spread of acid-gas plumes injected in deep saline aquifers in western Canada as an analogue for CO_2 injection into continental sedimentary basins, paper presented at 7th International Conference on Greenhouse Gas Control Technologies, SPONSOR, Vancouver, B. C., Canada.

Bakulin, A., and V. Korneev (2008), Acoustic signatures of cross flow behind casing in commingled reservoirs: A case study from Teapot Dome, *Geophysics*, *73*(4), E145–E152, doi:10.1190/1.2940154.

Barnes, D. A., W. B. Harrison, and A. Wahr (2008), Assessment of regional geological carbon sequestration potential in Upper Silurian to Middle Devonian strata of the Michigan Basin, in *Carbon Dioxide Sequestration in Geological Media—State of the Science*, edited by M. Grobe, J. C. Pashin, and R. L. Dodge, *AAPG Stud.*, 59, 1–26.

Biot, M. A. (1952), Propagation of elastic waves in a cylindrical bore containing a fluid, *J. Appl. Phys.*, *23*, 997–1005, doi:10.1063/1.1702365.

Biot, M. A. (1956), Theory of propagation of elastic waves in a fluid saturated porous solid. I. Low-frequency range, *J. Acoust. Soc. Am.*, *28*, 168–178, doi:10.1121/1.1908239.

Blackburn, E. A., L. Wilson, and R. S. J. Sparks (1976), Mechanisms and dynamics of Strombolian activity, *J. Geol. Soc.*, *132*, 429–440, doi:10.1144/gsjgs.132.4.0429.

Bohnhoff, M., G. Dresen, W. L. Ellsworth, and H. Ito (2010a), Passive seismic monitoring of natural and induced earthquakes: Case studies, future directions and socio-economic relevance, in *New Frontiers in Integrated Solid Earth Sciences, International Year of Planet Earth*, edited by S. Cloetingh and J. Negendank, pp. 261–285, doi:10.1007/978-90-481-2737-5_7, Springer, New York.

Bohnhoff, M., M. D. Zoback, L. Chiaramonte, J. Gerst, and N. Gupka (2010b), Seismic detection of CO_2 leakage along monitoring wellbores, *Int. J. Greenhouse Gas Control*, *4*, 687–697, doi:10.1016/j.ijggc.2010.01.009.

Celia, M., S. Bachu, J. M. Nordbotton, S. E. Gasda, and H. K. Dahle (2004), Quantitative estimation of CO_2 leakage from geological storage: Analytical models, numerical models, and data needs, paper presented at 7th International Conference on Greenhouse Gas Control Technologies, SPONSOR, Vancouver, B. C., Canada.

Chouet, B. (1988), Resonance of a fluid-driven crack: Radiation properties and implications for the source of long-period events and harmonic tremor, *J. Geophys. Res.*, *93*(B5), 4375–4400, doi:10.1029/JB093iB05p04375.

Chouet, B., P. Dawson, and M. Nakano (2006), Dynamics of diffusive bubble growth and pressure recovery in a bubbly rhyolitic melt embedded in an elastic solid, *J. Geophys. Res.*, *111*, B07310, doi:10.1029/2005JB004174.

Duguid, A., M. Radonjic, R. Bruant, T. Mandecki, G. Schere, and M. Celia (2004), The effect of CO_2 sequestration on oil well cements, paper presented at 7th International Conference on Greenhouse Gas Control Technologies, SPONSOR, Vancouver, B. C., Canada.

Espie, T. (2004), Understanding risk for the long term storage of CO_2 in geologic formations, paper presented at 7th International Conference on Greenhouse Gas Control Technologies, SPONSOR, Vancouver, B. C., Canada.

Intergovernmental Panel on Climate Change (IPCC) (2007), *Climate Change 2007: Mitigation of Climate Change*, edited by B. Metz et al., Cambridge Univ. Press, Cambridge, U. K. (Available at http://www.ipcc.ch/ipccreports/ar4-wg3.htm)

Julian, B. R. (1994), Volcanic tremor: Nonlinear excitation by fluid flow, *J. Geophys. Res.*, *99*, 11,859–11,877, doi:10.1029/93JB03129.

Neuberg, J., and R. Luckett (1996), Seismo-volcanic sources on Stromboli volcano, *Ann. Geophys.*, *39*(2), 377–391.

Nishimura, T. (1998), Source mechanisms of volcanic explosion earthquakes: Single force and implosive sources, *J. Volcanol. Geotherm. Res.*, *86*, 97–106, doi:10.1016/S0377-0273(98)00088-2.

Paillet, F. L., and C. H. Cheng (1991), *Acoustic Waves in Boreholes*, CRC Press., Boca Raton, Fla.

Powers, M. (2006), North Estes field in Texas: IEA Greenhouse Gas R&D Programme (IEA GHG), paper presented at 2nd Well Bore Integrity Network Meeting, Princeton Univ., Princeton, N. J.

Pruess, K. (2008), Leakage of CO2 from geologic storage: Role of secondary accumulation at shallow depth, *Int. J. Greenhouse Gas Control*, *2*, 37–46, doi:10.1016/S1750-5836(07)00095-3.

Riuscetti, M., R. Schick, and D. Seidl (1977), Spectral parameters of volcanic tremors at Etna, *J. Volcanol. Geotherm. Res.*, *2*, 289–298, doi:10.1016/0377-0273(77)90004-X.

Rutledge, J. T., W. S. Phillips, A. Roff, J. N. Albright, T. Hamilton-Smith, S. Jones, and K. Kimmich (1994), Subsurface fracture mapping using microearthquakes detected during primary oil production, Clinton County, Kentucky, paper SPE 28384 SPE Annual Technical Conference and Exhibition, Soc. of Pet. Eng., New Orleans, La., 25-28 Sept.

Schrag, D. P. (2007), Preparing to capture carbon, *Science*, *315*, 812–813, doi:10.1126/science.1137632.

Shapiro, S. A. (2008), *Microseismicity: A Tool for Reservoir Characterization*, Eur. Assoc. of Geosci. and Eng., Amsterdam, Netherlands.

Shearer, P. M. (1999), *Introduction to Seismology*, 260 pp., Cambridge Univ. Press, Cambridge, U. K.

Shimomura, Y., T. Nishimura, and H. Sato (2006), Bubble growth processes in magma surrounded by an elastic medium, *J. Volcanol. Geotherm. Res.*, *155*, 307–322, doi:10.1016/j.jvolgeores.2006.04.003.

Smolen, J. J. (1995), Fluid movement: Noise logging, in *Cased Hole and Production Log Evaluation*, pp. 255–268, PennWell Books, Tulsa, Okla.

Udias, A. (1999), *Principles of Seismology*, 475 pp., Cambridge Univ. Press, Cambridge, U. K.

Vavryčuk, V. (1992), Polarization properties of near-field waves in homogeneous isotropic and anisotropic media: Numerical modeling, *Geophys. J. Int.*, *110*, 180–190, doi:10.1111/j.1365-246X.1992.tb00720.x.

Vavryčuk, V. (1994), Elastic near-field wave energy radiated by a spherical cavity, *Rev. Mod. Phys.*, *66*(1), 241–247, doi:10.1103/RevModPhys.66.241.

Weichert, D., R. B. Horner, and S. G. Evans (1994), Seismic signatures of landslides: The 1990 Brenda Mine collapse and the 1965 hope rockslides, *Bull. Seismol. Soc. Am.*, *84*(5), 1523–1532.

White, J. E. (1983), *Underground Sound: Application of Seismic Waves*, *Methods Geochem. Geophys.*, vol. 18, Elsevier, Amsterdam.

M. Bohnhoff, Helmholtz Centre Potsdam, GFZ German Research Centre for Geosciences, Section 3.2, D424, Telegrafenberg, D-14473 Potsdam, Germany. (bohnhoff@gfz-potsdam.de)

M. D. Zoback, Department of Geophysics, Mitchell Building, Stanford University, Stanford, CA 94305-2215, USA.